



**HAL**  
open science

# Global modeling of iodine Hall thruster performance and discharge properties

Francesco M Bianchi, Alfio E Vinci, Laurent Garrigues

► **To cite this version:**

Francesco M Bianchi, Alfio E Vinci, Laurent Garrigues. Global modeling of iodine Hall thruster performance and discharge properties. *Journal of Applied Physics*, 2024, 137 (4), pp.043301. 10.1063/5.0244131 . hal-04906091

**HAL Id: hal-04906091**

**<https://hal.science/hal-04906091v1>**

Submitted on 22 Jan 2025

**HAL** is a multi-disciplinary open access archive for the deposit and dissemination of scientific research documents, whether they are published or not. The documents may come from teaching and research institutions in France or abroad, or from public or private research centers.

L'archive ouverte pluridisciplinaire **HAL**, est destinée au dépôt et à la diffusion de documents scientifiques de niveau recherche, publiés ou non, émanant des établissements d'enseignement et de recherche français ou étrangers, des laboratoires publics ou privés.

# Global modeling of iodine Hall thruster performance and discharge properties

Francesco M. Bianchi,<sup>1,2, a)</sup> Alfio E. Vinci,<sup>2, b)</sup> and Laurent Garrigues<sup>1, c)</sup>

<sup>1)</sup>LAPLACE, Université de Toulouse, CNRS, INPT, UPS, 31062, Toulouse, France

<sup>2)</sup>ThrustMe, Verrières-le-Buisson, 91370, France

(Dated: 11 December 2024)

A 0D model for an iodine-fed Hall thruster is presented. A complete set of reactions is used to account for iodine plasma chemistry phenomena and trace the presence of multiple neutrals and ionized species. The model is developed using novel assumptions based on experimental data trends as derived from the literature. The simulation domain is divided in two zones in order to refine the iodine molecule dissociation process localized in the low electron temperature region found upstream in the channel. After validating a xenon version of the model against SPT-100 characteristics, numerical results are compared against experimental data relative to a low-power iodine-fed Hall thruster. Discharge current and thrust are predicted with satisfactory quantitative agreement and overall trends are effectively captured. The numerical results indicate a relatively large portion of ionized molecules, while negative ions appear to occur in non-negligible amount upstream in the thruster channel.

## I. INTRODUCTION

Propellants with a low ionization threshold, large ionization threshold and high atomic mass are sought-after in order to maximize thrust-to-power ratio of electrostatic propulsion devices. These aspects historically led to the utilization of xenon in gridded ion thrusters and Hall thrusters. Its scarce natural occurrence in the current context of industrial production capacity versus market demand, however, leads to significant price fluctuations over a large baseline price, often determinant for typical commercial missions. Propulsion systems utilizing alternative propellants have been already deployed in orbit. At the time of writing, the Starlink constellation counts more than 4700 krypton-fed and more than 1600 argon-fed Hall thruster systems in orbit. These solutions, however, sacrifice thrust-to-power ratio due to the lower atomic mass of the chosen propellants. On the other hand, iodine-fed propulsion systems provide significant advantages over both xenon and other noble gases. Iodine provides the same performance achievable with xenon at 1 – 2% the cost. Furthermore, while xenon-fed systems require the propellant to be stored at high pressures (14 MPa - 20 MPa) at relatively low storage density ( $1.6 \text{ g cm}^{-3}$ ), iodine is stored solid, resulting in a higher storage density ( $4.9 \text{ g cm}^{-3}$ )<sup>1</sup> and without the need of high pressure rated hardware. These factors have thus driven an increased interest in iodine<sup>2,3</sup>. While iodine-fed gridded ion thrusters is a proven and viable technology for very low power systems<sup>4</sup>, Hall thrusters (HTs) become increasingly attractive at higher power levels, as they feature higher thrust-to-power ratios and a higher thrust density. With this in mind, iodine-fed HTs have been previously tested at different power ranges undertaken<sup>5,6</sup> and ThrustMe has set out to develop a low-power iodine-fed HT<sup>7</sup>.

One of the main challenges in the development of an iodine HT is to grasp the plasma chemistry. As iodine is present in both atomic and molecular forms, and given the electronegative nature of iodine, a larger variety of species are found in the plasma when compared to devices using noble gases. Studies of this type are scarce in the literature, and previous efforts have been largely focused on iodine-fed ion thrusters and fundamental plasma discharges<sup>8–10</sup>, where however electron temperature never exceeds a few electronvolt, leading to different phenomena being more relevant in comparison with HTs, where electron temperature can reach tens of electronvolts. 0-D models represent a powerful tool for the purpose of plasma chemistry studies and global thruster metrics estimation. HTs have been previously modeled through a 0D framework, though mostly in order to shed light on breathing mode oscillations in xenon-fed thrusters<sup>11–14</sup>. Consequently, it is necessary to analyze iodine HT to estimate energy losses caused by plasma processes and thruster performance.

This paper focuses on analyzing the global effects of iodine chemistry on thruster performance through the development of a 0D model. Section II introduces the set of equations and plasma chemistry utilized in the model. Section III reports on the assumptions made in order to implement the conservation equations. Section IV presents and discuss numerical results of the model, simulating both xenon and iodine-fed HTs, through comparison with experimental data. Finally, in Section V conclusions are provided.

## II. NUMERICAL MODELING

### A. Domain

The model domain is comprised of two 0D zones. A first zone, called the dissociation zone, extends from the anode to a fraction of the channel, where only low temperature electrons are typically found. Using literature data<sup>15–18</sup>, it is deduced that this length can be assumed to be  $0.425 L_{ch}$  from the anode plane, with  $L_{ch}$  being the channel length. Due to the low electron temperature plasma found in the dissociation zone,

<sup>a)</sup>PhD Candidate, ThrustMe (associated with LAPLACE, Université de Toulouse), francesco.bianchi@thrustme.fr

<sup>b)</sup>Plasma Physicist, ThrustMe, alfo.emanuele.vinci@thrustme.fr

<sup>c)</sup>Director of Research at CNRS, LAPLACE, laurent.garrigues@laplace.univ-tlse.fr

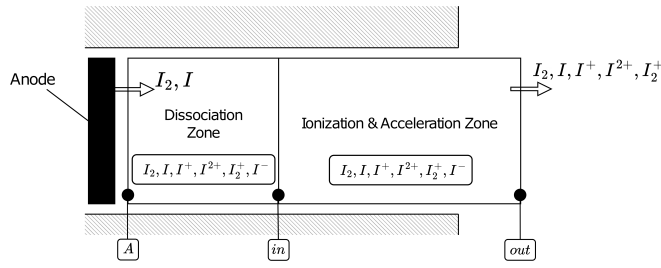


FIG. 1. Schematic of the simulation domain with the two zones high-120  
lighted.

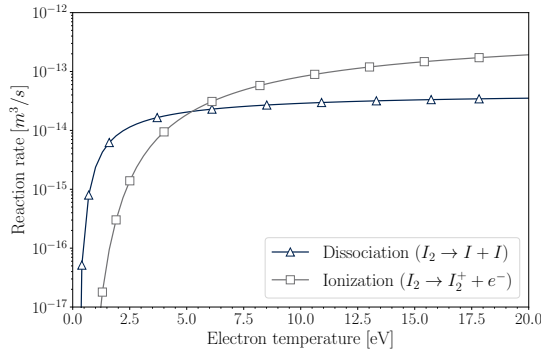


FIG. 2. Reaction rate of ionization and dissociation of the iodine<sup>134</sup>  
molecule. Based on data of Lafleur<sup>10</sup> and Esteves<sup>9</sup>.

84 only dissociation of neutral iodine molecules  $I_2$  and formation  
85 of negative ions  $I^-$  are taken into consideration. Other reac-<sup>137</sup>  
86 tions are assumed to play a negligible role due to their high<sup>138</sup>  
87 threshold, as noted in Table I. The second zone extends from<sup>139</sup>  
88  $0.425 L_{ch}$  to  $1.2 L_{ch}$ . In this zone the ionization and accelera-<sup>140</sup>  
89 tion phenomena are addressed.

90 Preliminary tests of the model that accounted for dissocia-<sup>142</sup>  
91 tion, ionization and acceleration in a single zone revealed that,<sup>143</sup>  
92 as a consequence of the global nature of the model, the beam<sup>144</sup>  
93 would be primarily composed of ionized molecules, resulting<sup>145</sup>  
94 from a relatively low dissociation rate. This is in contrast with<sup>146</sup>  
95 some experimental evidence<sup>19</sup>. The use of a single node al-<sup>147</sup>  
96 lows high temperature electron to ionize a large proportion<sup>148</sup>  
97 of molecules before they are dissociated, due to ionization<sup>149</sup>  
98 having a higher reaction rate for  $T_e > 5$  eV, as shown in Fig.2.<sup>150</sup>  
99 From experimental and numerical data<sup>17,18</sup>, it is expected that<sup>151</sup>  
100 low temperature electrons are found in the upstream half of<sup>152</sup>  
101 the discharge channel causing neutral molecules to preferably<sup>153</sup>  
102 dissociate. Eventually, as the flow of neutrals reaches the ion-<sup>154</sup>  
103 ization and acceleration zone, a relatively small fraction of<sup>155</sup>  
104 molecules is present, leading to only an ion beam primarily<sup>156</sup>  
105 composed of atomic ions, with a smaller group of molecular<sup>157</sup>  
106 ions ( $I_2^+$ ). The separation of the domain in two zones allows<sup>158</sup>  
107 for molecules to be first dissociated in the first zone without<sup>159</sup>  
108 being ionized by the high temperature electrons found in the<sup>160</sup>  
109 second zone, reflecting the spatial separation found in the dis-<sup>161</sup>  
110 charge channel.

## 112 B. Equations

113 The core of the model consists in the numerical integra-  
114 tion of ordinary differential equations (ODEs). These equa-  
115 tions are evaluated and propagated in time through Euler for-  
116 ward integration. All equations are integrated simultaneously.  
117 At each timestep, algebraic equations are also solved, both  
118 for post-processing purposes and to calculate source and sink  
119 terms found in the right-hand side of the ODEs. A constant  
120 timestep of  $6 \times 10^{-8}$  s is used. All simulation are run for 1 ms,  
121 after which convergence is confirmed by ensuring that the  
122 variation of the main plasma properties between steps does not  
123 exceed 0.001%. The plasma is assumed to be quasi-neutral,  
124 electron inertia is considered negligible, neutrals are assumed  
125 to have a constant velocity and all heavy species (neutrals and  
126 ions) are considered cold. The ODEs are obtained through do-  
127 main integration of a fluid 1D1V model, similar to those found  
128 in Refs.[17, 20]. In the dissociation zone, a set of continuity  
129 equations are propagated. In the ionization and acceleration  
130 zone, continuity, momentum, electron energy equations are  
131 propagated. Additionally, an electrostatic relation is solved at  
132 each timestep.

### 133 1. Continuity in dissociation zone

134 In the dissociation zone a set of simplified continuity dif-  
135 ferential equations are integrated, accounting only for neutral  
136 and negative species ( $\alpha = \{I_2, I, I^-\}$ ). These equation read:

$$\frac{\partial \bar{n}_{\alpha,diss}}{\partial t} = - \left( \frac{1}{L_{diss}} \right) (n_{in,\alpha} u_{z,in,\alpha} - n_{A,\alpha} u_{z,A,\alpha}) + \bar{S}_{coll,\alpha,diss}, \quad (1)$$

where  $\bar{n}_{\alpha,diss}$  indicates the average numerical density of  
species  $\alpha$  in the dissociation zone,  $A$  indicates the anode,  $L_{diss}$   
the length of the dissociation zone. At each timestep, the con-  
tinuity equations are integrated to obtain the average numeri-  
cal density of the considered species within the dissociation  
zone. By assuming constant velocity and a linear spatial dis-  
tribution within the dissociation zone, the densities of  $I$  and  
 $I_2$  at the entrance of the ionization zone can then be derived.  
They are dependent of the rate of dissociation and dissociative  
electron detachment.

Negative ions are assumed to be generated and removed  
from the dissociation zone entirely through collisions, there-  
fore neglecting any flux term of  $I^-$  towards the ioniza-  
tion/acceleration zone. Negative ion flux towards the anode  
and the channel walls is also neglected, due to the presence  
of positive ion sheaths. Thus, for the purposes of this model,  
 $\{u_{z,A,I^-}, u_{z,in,I^-}\} = 0$ .

In order to calculate  $\bar{S}_{coll,\alpha,diss}$ , the plasma density in the  
dissociation zone must be known. Given the lack of experi-  
mental data regarding electric field magnitude in the upstream  
half of the discharge channel, estimation of electron transport  
is difficult. To avoid the introduction of modeling errors, a  
simple assumption is taken: the plasma density in the dissoci-  
ation zone is assumed to be a fraction of the average plasma  
density in the ionization and acceleration zone. This is sup-

ported by experimental and numerical data<sup>21,22</sup>, which indicate that plasma density in the upstream half of the discharge channel is roughly one order of magnitude lower than that in the ionization region. Said ratio is then represented by an arbitrary coefficient,  $\beta_{diss}$ :

$$n_{plasma,diss} = \beta_{diss} \bar{n}_{plasma}, \quad (2)$$

where  $n_{plasma,diss}$  is the plasma density in the dissociation zone and  $\bar{n}_{plasma}$  is the average plasma density in the ionization and acceleration zone. The coefficient  $\beta_{diss}$  is then swept between two extreme values, 0.1 and 0.75, representing the uncertainty surrounding plasma density deep in the channel. When calculating the collision rate in the dissociation zone, in order to account for the presence of negative ions, electron density is assumed to be equal to:

$$n_{e,diss} = n_{plasma,diss} - n_{I^-,diss}. \quad (3)$$

Note that this parameter affects the plasma density in the dissociation zone, which is assumed to be equal to that at the *in* boundary, consequently affecting the dissociation process. This has an important influence on the composition of the plasma beam, and the effects of  $\beta_{diss}$  on the model results are discussed in Section IV. Continuity equations relative to the dissociation zone are integrated at each time step to provide the equations modeling ionization and acceleration with the necessary boundary conditions.

## 2. Continuity in the ioniz./acc. zone

A continuity equation is solved for all species, both charged and neutral. Electron density is calculated from quasi-neutrality, and as such does not require the integration of a dedicated ODE. Analytical integration of the generalized continuity equation<sup>20</sup> leads to the expression:

$$\frac{\partial \bar{n}_\alpha}{\partial t} = - \left( \frac{1}{L} \right) (n_{out,\alpha} u_{z,out,\alpha} - n_{in,\alpha} u_{z,in,\alpha}) + \bar{S}_{w,\alpha} + \bar{S}_{coll,\alpha}, \quad (4)$$

where  $\alpha = \{I_2, I, I_2^+, I^+, I^{2+}, I^-\}$  or  $\alpha = \{Xe, Xe^+, Xe^{2+}\}$ ,  $n$  is the numerical density,  $u_z$  is the velocity along the thruster's axis,  $S_w$  is the flux of particles to the walls,  $S_{coll}$  is the rate of particles lost or generated due to collisions, *out* and *in* indicate the end and start respectively of the ionization and acceleration zone, with  $L$  being its length (see Fig.1).

## 3. Momentum in the ioniz./acc. zone

Following the generalized momentum conservation equation<sup>20</sup>, the scalar global momentum conservation equation for heavy species reads:

$$\frac{\partial}{\partial t} \underbrace{\bar{n}_\alpha u_{z,\alpha}}_{\text{momentum}} = - \underbrace{(1/L)(n_{\alpha,out} u_{z,\alpha,out}^2 - n_{\alpha,in} u_{z,\alpha,in}^2)}_{\text{convection}} + \underbrace{\bar{n}_\alpha \frac{q_\alpha}{m_\alpha} \bar{E}_z}_{\text{electric field}}, \quad (5)$$

where  $E_z$  is the electric field along the thruster axis,  $q$  is the particle charge and  $m$  is its mass. Note that  $\bar{n}_\alpha \bar{E}_z \neq n_\alpha E_z$ , as both  $n_\alpha$  and  $E_z$  vary along  $z$ . However, as the exact value of  $\bar{n}_\alpha \bar{E}_z$  cannot be calculated within a 0D framework, and approximation is necessary, and a product of averages is instead used. In this model,  $\bar{E}_z = 0.88V_d/L$ , with  $V_d$  being the anode potential. This choice is coherent with the assumptions taken on ion velocity shape within the domain shown in Section III. Neutral momentum is not resolved, and their velocity is considered constant in time and equal to a fraction of thermal velocity at the anode as verified by prior Monte-Carlo simulations<sup>7</sup>, and to sonic velocity at the end of the domain.

## 4. Energy in the ioniz./acc. zone

The conservation of energy is solved for the electrons.

$$\frac{\partial}{\partial t} \underbrace{\left( \frac{3}{2} k_B \bar{n}_e T_e \right)}_{\text{internal energy}} = \underbrace{- \frac{5}{2} (1/L) (n_{e,out} k_B T_{e,out} u_{e,z,out} - n_{e,in} k_B T_{e,in} u_{e,z,in})}_{\text{convection}} + \underbrace{\frac{(JA_{ch} 0.88V_d - P_{beam})}{A_{ch} L}}_{\text{electric field}} - \underbrace{\bar{S}_{en,coll}}_{\text{collisions}} - \underbrace{\bar{S}_{en,wall}}_{\text{wall losses}}, \quad (6)$$

where  $k_B$  is the Boltzmann constant,  $T_e$  is the electron temperature,  $S_{en,coll}$  is the energy lost to collisions,  $S_{en,wall}$  is the energy lost to channel walls and  $(JA_{ch} 0.88V_d - P_{beam})/(A_{ch} L)$  is the contribution of the electric field with  $J$  being the current density,  $A_{ch}$  the channel cross section and  $P_{beam}$  the beam power. The power delivered to the electron via the electric field can in principle be approximated as  $\bar{n}_e \bar{u}_{e,z} \bar{E}_z$ , yet this was found to introduce a large error, leading to unrealistic amounts of power delivered to the electrons. This error has been attributed to the largely non-constant nature of the spatial distributions of  $n_e(z)$ ,  $E_z(z)$ ,  $u_{e,z}(z)$ , leading to a large difference between the exact integral  $\bar{n}_e \bar{u}_{e,z} \bar{E}_z$  and the approximation  $\bar{n}_e \bar{u}_{e,z} \bar{E}_z$ . The contribution of the electric field is then calculated by subtracting the beam power from the total discharge power (as seen in Fig.3). The beam power is calculated as:

$$P_{beam} = \sum_{\alpha} \frac{1}{2} n_{\alpha,out} m_{\alpha} u_{z,\alpha,out}^3 A_{ch}, \quad (7)$$

with  $\alpha = \{I^+, I^{2+}, I_2^+\}$ .

Conduction and pressure terms are not considered, as their relevance becomes secondary in a global model. While local gradients in the electron temperature may be locally significant, their contribution to overall electron energy is a few orders of magnitude lower than other more significant terms. This is also reflected in the work of Lafleur et al.<sup>11</sup>.

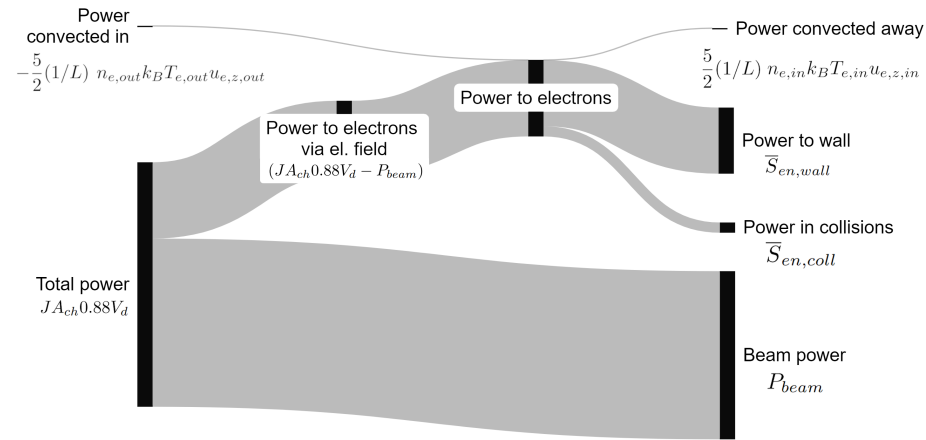


FIG. 3. Example of distribution of power within the simulation domain.

## 247 5. Electrostatic relation

248 The electrostatic relation is utilized to obtain the current  
249 density, which is used in the conservation of electron energy.  
250 It is derived from the electron momentum conservation equa-  
251 tion, where the inertia has been considered negligible and it is  
252 referred to as Ohm's law<sup>23</sup>. The current density  $J$  is defined  
253 as:

$$254 J = q_e \left( \sum_{\alpha} Z_{\alpha} n_{\alpha} u_{z,\alpha} \right) - q_e n_e u_{z,e} = \sum_{\alpha} j_{z,\alpha} - j_{z,e}, \quad (8) \quad 281$$

255 where  $Z$  is the charge number and  $\alpha$  represents the various  
256 charged heavy species. Within a fluid 1D framework, the cur-  
257 rent density  $J$  can be considered spatially constant if the chan-  
258 nel walls are dielectric. As a consequence of said property, an  
259 integral form of Ohm's law can be used. The relation used by  
260 Giannetti et al.<sup>17</sup> in their 1D1V fluid model can in principle  
261 be formulated in a 0D framework, reading:

$$262 J = q_e \mu_e \bar{n}_e \frac{\Delta V}{L} + q_e \sum_{\alpha} (\bar{u}_{z,\alpha} \bar{n}_{\alpha} Z_{\alpha}) + \mu_e \overline{\nabla(n_e k_B T_e)}, \quad (9) \quad 288$$

263 where  $\mu_e$  is the electron mobility and  $\Delta V$  is the total poten-  
264 tial drop across the domain, accounting for the anode sheath  
265 potential, which is assumed to be electron repelling. This for-  
266 mulation did however lead to large underestimations of the  
267 current density, potentially caused by the large approxima-  
268 tions errors generated in the management of the product of  
269 averages, as mentioned before. As a consequence, Ohm's law  
270 is evaluated at the end of the domain, again exploiting the as-  
271 sumption of a spatially constant current density:

$$272 J = q_e n_{e,out} \mu_{e,out} E_{z,out} - \mu_{e,out} k_B \left. \frac{dn_e T_e}{dz} \right|_{out} + \quad 298$$

$$273 + \sum_{\alpha} Z_{\alpha} q_e n_{\alpha,out} u_{z,\alpha,out} \quad (10) \quad 299$$

274 where the electron mobility  $\mu_{e,out}$  accounts for anomalous  
275 transport by assuming Bohm-like transport, as previously em-  
276 ployed in literature<sup>24</sup>:

$$v_e = v_{classical} + \beta_{an} \frac{\omega_e}{16}, \quad (11)$$

277 where  $\nu$  is the collision frequency and  $\omega_e$  is the electron cy-  
278 clotron frequency. For all cases simulated  $\beta_{an} = 0.1$  was uti-  
279 lized. A more complex model of anomalous transport cannot  
280 be justified, given the limited nature of a global model. The  
281 electric field at the end of the domain has been estimated as:

$$E_{z,out} = \frac{0.25 \Delta V}{0.29 L_{ch}}. \quad (12)$$

This assumption is based on the considerations made in  
Refs.[25,26] concerning the location and the spatial extension  
of the acceleration zone as functions of anode potential and  
channel length.

## C. Plasma chemistry

The model presented implements either iodine or xenon  
chemistry, and, as such, two set of reactions are presented.  
Only binary reactions involving collision between an electron  
and a heavy species are considered. Charge exchange reac-  
tions are ignored, due to the 0D nature of the model which  
cannot grasp local velocity difference between species. When  
modeling iodine-fed systems, the following species are con-  
sidered:  $I_2, I, I_2^+, I^+, I^{2+}, I^-$ . When modeling xenon-fed sys-  
tems, the following species are considered:  $Xe, Xe^+, Xe^{2+}$ .

### 1. Calculation of particles generation rate

The averaged continuity source/sink is approximated in the

300 following manner:

$$\bar{S}_{coll,\alpha} = \sum_{reactions} \bar{n}_e \bar{n}_{target} \bar{K}_{reaction}(T_e) - \sum_{reactions} \bar{n}_e \bar{n}_\alpha \bar{K}_{reaction}(T_e), \quad (13)$$

301 where  $K_{reaction}$  is the reaction rate of a given reaction and  $n_{target}$  is the density of the species that is impacted by an elec-  
302 tron to generate  $\alpha$ . The average densities are directly found  
303 by the integration in time of the continuity equation. The av-  
304 erage reaction rate is calculated using an approach detailed in  
305 section III. Please note the difference between the average of  
306 the maxwellian distribution  $T_e$  (local property) and the aver-  
307 age electron temperature in the domain  $\bar{T}_e$ , which is the spatial  
308 average of the former.

309 Reaction rates are calculated from cross section curves after  
310 integration over a Maxwellian distribution. Which are avail-  
311 able from experimental data<sup>27-29</sup>, numerical data<sup>30-32</sup> and nu-  
312 merical calculations performed during the development of this  
313 model. All the reactions considered are presented in Table  
314 I and Table II. The cross sections that have been calcu-  
315 lated in this work exploit the method presented in Belenger  
316 et al.<sup>33</sup>, used to estimate the cross section of multiple ion-  
317 ization events. This method was at first validated for iodine  
318 by comparing its results with the cross section of the double  
319 ionization of the iodine atom ( $I + e^- \rightarrow I^{2+} + 3e^-$ ) measured  
320 experimentally by Hayes et al.<sup>27</sup>.

## 323 2. Calculation of electron energy collision sinks

324 The energy lost by electrons in elastic collisions is esti-  
325 mated by<sup>9,10</sup>:

$$\bar{S}_{en,coll,el} = \sum_{neutrals} 3 \frac{m_e}{m_n} k_B \bar{T}_e \bar{n}_n \bar{n}_e \bar{K}_{el.,n}(T_e), \quad (14)$$

327 where  $n = \{ I, I_2 \}$  or  $n = \{ Xe \}$ . The energy lost in inelastic  
328 collisions is:

$$\bar{S}_{en,coll,inel} = \sum_{reactions} \varepsilon_{ij} \bar{n}_i \bar{n}_j \bar{K}_{ij}(T_e), \quad (15)$$

330 where  $\varepsilon_{ij}$  is the threshold energy for a reaction with  $i$  as a  
331 reagent and  $j$  as a product. This is a constant value except  
332 for excitation reactions, where an effective level is used, with  
333 the cumulative cross section of all excitations, the energy  
334 of which is adjusted with electron temperature to represent  
335 different excitation processes with different thresholds. Ex-  
336 citation reactions are only considered as an energy sink, as  
337 metastable states are not tracked species, as previously done  
338 by Lafleur<sup>10</sup>.

## 339 D. Wall interaction

340 Two types of wall interaction are considered in this model:  
341 charged species falling through the sheath and neutral iodine  
342 atoms recombining into a molecule at the wall. The energy  
343 deposited by electrons impacting wall is also calculated.

## 344 1. Wall collision rate for charged species

The wall interaction frequency is calculated for each ion  
species having positive charge, since negative ions are rep-  
elled by the sheath. For each ion species, the loss to the  
wall is calculated as:

$$\bar{S}_{w,\alpha} = - \left[ \frac{(1-0.425)L_{ch}}{(1.2-0.425)L_{ch}} \right] \alpha_w \exp(0.5) \bar{n}_\alpha \frac{2}{\Delta R} \sqrt{\frac{Z_\alpha k_B \bar{T}_e}{m_\alpha}}, \quad (16)$$

where the first term scales the wall losses according to the  
fraction of the domain that is inside of the channel,  $\Delta R$  is the  
difference between outer and inner radius of the channel,  $\alpha_w$   
is a calibration factor which has been set to 0.11 as done by  
Leporini et al.<sup>12</sup>. The  $\exp(0.5)$  term accounts for the density  
at the sheath edge being lower than the bulk density due to  
presheath acceleration<sup>36</sup>. The  $2/\Delta R$  term is the result of the  
volume averaging and accounts for thruster geometry. The  
last term, under the square root, is the Bohm ion velocity.  
For each ion impacting the wall, a neutral of the same species  
is emitted and inserted back into the simulation domain.

## 345 2. Wall recombination

346 In iodine chemistry wall recombination is also considered,  
347 where two neutrals atom impacting the wall can recombine  
348 into a molecule:



Lafleur et al.<sup>10</sup>, among others, model wall recombination with  
a sticking probability factor  $\gamma_w$ . The recombination rate is then  
calculated as:

$$\bar{S}_{wall,I,recomb} = - \frac{2}{\Delta R} \frac{1}{4} \bar{n}_I u_{th,I} \left( \frac{2\gamma_w}{2-\gamma_w} \right), \quad (18)$$

$$\bar{S}_{wall,I_2,recomb} = + \frac{1}{2} \bar{S}_{wall,I,recomb}, \quad (19)$$

where  $u_{th,I}$  is the atom thermal velocity and  $\gamma_w$  is the wall  
sticking probability.

## 349 3. Electron energy deposition to wall

The power delivered to the walls of the discharge channels  
by electrons is calculated as:

$$\bar{S}_{en,wall} = \bar{n}_e \exp(0.5) \bar{v}_{e,w} \bar{\varepsilon}_{wall}, \quad (20)$$

where  $v_{e,w}$  is the wall collision frequency,  $\varepsilon_{wall}$  is the energy  
associated with each electron. As the channel walls are as-  
sumed dielectric, the electron wall collision frequency can be  
calculated by balancing the flux of positive ions to the wall  
with the flux of electrons, keeping secondary electron emis-  
sion in mind:

Name	Reaction	Threshold [eV]	Source/Comments
Elastic	$I + e^- \rightarrow I + e^-$	0	Ref. 30
Excitation	$I + e^- \rightarrow I^* + e^-$	[0.9426 - 8.14]	Combined curve from Ambalampitiya et al. <sup>30</sup> , threshold energy is adjusted in 4 steps to represent 4 groups of possible excitations.
Ionization	$I + e^- \rightarrow I^+ + 2e^-$	10.45	Ref. 27
Double Ionization	$I + e^- \rightarrow I^{2+} + 3e^-$	29.58	Ref. 27
Elastic	$I_2 + e^- \rightarrow I_2 + e^-$	0	Numerical data from Ambalampitiya et al. <sup>30</sup> up to 10 eV. Trend after 10 eV is $1/E$ as in Esteves <sup>9</sup> .
Elastic momentum	$I_2 + e^- \rightarrow I_2 + e^-$	0	Ref. 30
Ionization	$I_2 + e^- \rightarrow I_2^+ + 2e^-$	9.31	Ref. 30 and 31
Dissociative ionization	$I_2 + e^- \rightarrow I^+ + I_{3/2} + 2e^-$	11.94	Ref. 30
Dissociative Attachment	$I_2 + e^- \rightarrow I^- + I_{3/2}$	0	Numerical data from Ambalampitiya et al. Ref. 30 up to 20 eV, power law after as done by Esteves <sup>9</sup> .
Dissociation	$I_2 + e^- \rightarrow 2I_{3/2} + e^-$	1.542	Numerical data from Esteves <sup>9</sup> up to 10 eV, after which a $\log(E)/E$ law is used, as done by Esteves <sup>9</sup> .
Excitation	$I_2 + e^- \rightarrow I_2^* + e^-$	2.18	Numerical data from Ambalampitiya et al. <sup>30</sup> up to 15 eV and a $1/E^2$ law after, as done by Esteves <sup>9</sup> .
Negative Ion Detachment	$I^- + e^- \rightarrow I_{3/2} + 2e^-$	3.059	Numerical data from Esteves <sup>9</sup> is used, though found to be potentially inaccurate due to lack of data points near the threshold and a very high cross section when compared to similar species.
Ionization from anion	$I^- + e^- \rightarrow I^+ + 3e^-$	13.5	This work.
Triple ionization from anion	$I^- + e^- \rightarrow I^{2+} + 4e^-$	32.64	This work.
Second Ionization	$I^+ + e^- \rightarrow I^{2+} + 2e^-$	29.58	Ref. 27
Ion dissociation	$I_2^+ + e^- \rightarrow I^+ + I + e^-$	2.1768	Ref. 34

TABLE I. Set of reactions considered in the iodine chemistry model.

Name	Reaction	Threshold [eV]	Comments
Ionization	$Xe + e^- \rightarrow Xe^+ + 2e^-$	12.13	Numerical data from LXCat, Hayashi database <sup>35</sup> .
Double Ionization	$Xe + e^- \rightarrow Xe^{2+} + 3e^-$	32.64	Ref. 28
Ionization of ion	$Xe^+ + e^- \rightarrow Xe^{2+} + 2e^-$	20.98	Ref. 29
Excitation	$Xe + e^- \rightarrow Xe^* + e^-$	[8.32 - 10.40]	Cumulative curve for all excitations. Numerical data from LXCat, Morgan database <sup>32</sup> . Threshold energy is picked among selection [8.44, 9.57, 9.917, 10.40] to represent different types of excitation

TABLE II. Set of reactions considered in the xenon chemistry model.

$$\sum_{\alpha=ions} Z_{\alpha} n_{\alpha} v_{\alpha,w} = n_e v_{e,w} (1 - \sigma_{SEE}), \quad (21)$$

$$\bar{\epsilon}_{wall} = 2k_B \bar{T}_e + \bar{\phi}_{wall}, \quad (23)$$

$$\begin{aligned} \bar{v}_{e,w} &= \bar{v}_{i,w} \frac{1}{1 - \sigma_{SEE}} = \\ &= \sum_{\alpha=ions} \alpha_{w,\alpha} Z_{\alpha} \left( \frac{\bar{n}_{\alpha}}{\bar{n}_e} \right) \sqrt{\frac{Z_{\alpha} k_B \bar{T}_e}{m_{\alpha}}} \left( \frac{2}{\Delta R} \right) \frac{1}{1 - \sigma_{SEE}}, \end{aligned} \quad (22)$$

where the secondary electron emission yield  $\sigma_{SEE}$  is calculated following the expression recommended by Goebel and Katz<sup>37</sup>. The energy associated with each electron can be calculated as:

where  $\phi_{wall}$  is the sheath potential. For a plasma with multiple positively charged species, we can derive the sheath potential by assuming a collisionless pre-sheath and sheath. In said sheath, each ion reaches the pre-sheath/sheath boundary at Bohm velocity. By equating the total ion current flux (derived from the Bohm velocity) at the wall with the electron current flux (due to the dielectric walls assumption), and utilizing Boltzmann's relation, it is possible to derive an integral equation to calculate the domain-average sheath potential:

$$\bar{\phi}_{wall} = \frac{k_B \bar{T}_e}{q_e} \ln \left( \frac{1}{1 - \sigma_{SEE}} \frac{1}{\bar{n}_e} \sqrt{2m_e} \sum_{ions} Z_{ion} \bar{n}_{ion} \sqrt{\frac{Z_{ion}}{m_{ion}}} \right). \quad (24)$$

### III. MODELING APPROACH

The differential equations at the core of the model propagate the extensive properties, such as the average momentum of  $I^+ \bar{n}_{I^+} m_{I^+} u_{z,I^+}$ . However, it is of interest to infer the intensive properties for linking the two modeled zones and for the sake of modeling itself. There is also a need to correlate an average value with physically appropriate boundary values. In summary, given the extensive properties obtained by integrating the ODEs, it is necessary to obtain intensive average plasma properties and boundary values of plasma properties. A solution utilized in the literature<sup>11,12</sup> is a constant or linear spatial distribution of plasma properties along the axis of the domain. For example, by assuming  $\bar{n} = n(z) = const.$ , it is then possible to derive:

$$\bar{n} \bar{u}_z = \bar{n} \bar{u}_z, \quad (25)$$

$$n_{out} = \bar{n}, \quad (26)$$

this, however, introduces large errors. For example, the steady state solution of the momentum equation becomes:

$$u_{z,\alpha,out} = \sqrt{\frac{\bar{n}_\alpha q_e \Delta V}{n_{\alpha,out} m_\alpha}} = \sqrt{\frac{q_e \Delta V}{m_\alpha}}, \quad (27)$$

which is equivalent to a voltage efficiency of  $\eta_v = 0.5$ , much lower than what typically found in HTs, i.e.  $\eta_v \approx 0.8$ . This can explain the low ion drift velocity predicted by the 0D model of Lafleur et al.<sup>11</sup>. Similarly, while early works of Leporini et al.<sup>12</sup> assumed a spatially constant plasma density, their most recent work<sup>38</sup> makes use of a set of arbitrary coefficients within the ODEs, with the goal of correcting the errors discussed above.

#### A. Assumptions on spatial distribution of plasma properties

In order to correlate the extensive plasma properties with their intensive counterparts, experimental and numerical data have been analyzed to identify trends in the spatial distribution of plasma properties in unshielded HTs. These trends have been condensed into a set of normalized curves  $T_e(z)$ ,  $u_z(z)$  and  $n(z)$  which allow to find a relation between  $\bar{n} \bar{u}_z$ ,  $\bar{n} \bar{T}_e$  and  $(\bar{n}, \bar{u}_z, \bar{T}_e)$ . These curves do not provide any local information on plasma properties, as they are merely a representation of the global trends, exploiting similarities in spatial distribution of plasma properties among unshielded HTs.

Due to the lack of experimental data observing plasma density inside the discharge channel, numerical data from Adam et al.<sup>39</sup> is used.

The normalized curves are scaled to represent a variety of

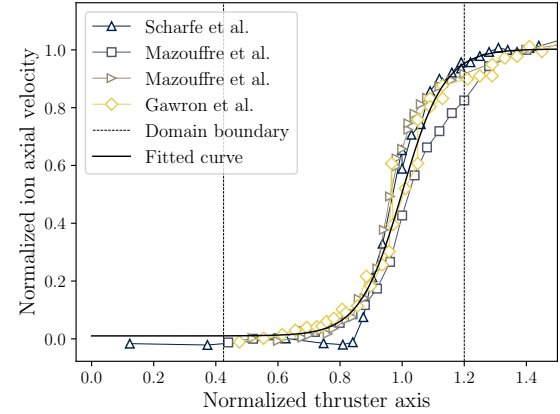


FIG. 4. Normalized curve of ion velocity. Experimental data from Scharfe et al.<sup>21</sup>, Mazouffre et al.<sup>40</sup>, Mazouffre et al.<sup>41</sup> and Gawron et al.<sup>42</sup>.

possible  $\bar{n}$ ,  $\bar{u}_z$  and  $\bar{T}_e$  values and eventually combined to associate each  $(\bar{n}, \bar{n} \bar{u}_z)$  tuple with the relevant  $\bar{u}_z$ , and each  $(\bar{n}, \bar{n} \bar{T}_e)$  with the relevant  $\bar{T}_e$ . Normalized curves are shown in Fig.4 and Fig.5 for ion velocity and electron temperature, respectively. The ion density curve is modeled as two matched gaussian curves:

$$n(z) = \begin{cases} a \frac{s_l}{s_r} \frac{1}{\sqrt{2\pi s_l}} \exp \left[ -0.5 \left( \frac{z-c}{s_l} \right)^2 \right] + 0.3a & \text{if } z < c \\ a \frac{1}{\sqrt{2\pi s_r}} \exp \left[ -0.5 \left( \frac{z-c}{s_r} \right)^2 \right] + 0.3a & \text{if } z > c, \end{cases} \quad (28)$$

with  $c = 0.84$ ,  $s_l = 0.225$ ,  $s_r = 0.092$ , and where  $a$  is a scaling factor. The ion velocity curve is modeled as a sigmoid:

$$u_z(z) = \frac{u_{fin}}{1 + \exp(-kz_0) \exp(-kz)} + b. \quad (29)$$

The two parameters affecting the shape of the sigmoid function  $k, b$  are obtained by running a fitting function which numerically fits the sigmoid curve to two points:  $u_z = 0$  at  $z = 0$  and  $u_z = 0.95 u_{fin}$  at  $z = 1.5 L_{ch}$ . The center of the sigmoid function,  $z_0$ , is set at 1 for all of the tests reported here, but could however be modified in future versions to adjust the assumed position of the acceleration zone. The final velocity  $u_{fin}$  is used as a scaling factor. Given the normalized curve obtained, the ions reach the end of the domain with the velocity equivalent to 0.88 of the total potential drop  $V_d$ . This value is then used in the conservation of momentum to estimate the average electric field, as previously discussed.

The electron temperature curve is modeled as two matched gaussian curves:

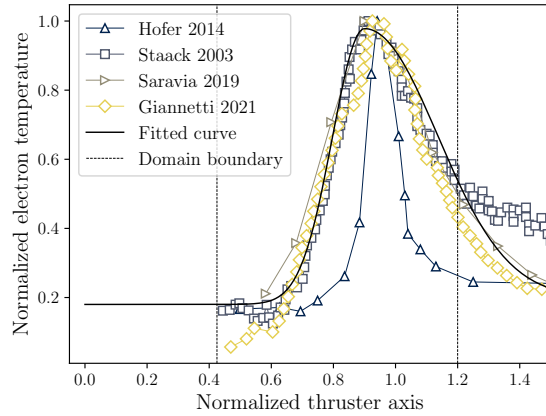


FIG. 5. Normalized curve of electron temperature. Experimental data is taken from Hofer et al.<sup>18</sup>, Staack et al.<sup>43</sup>, Saravia et al.<sup>16</sup> and Giannetti et al.<sup>17</sup>.

$$T_e = \begin{cases} a \cdot a_0 \left( \frac{1}{\sqrt{2\pi}s} \right) \exp \left[ -b_l \left( \frac{z-c}{s} \right)^2 \right] + T_{e,A} & \text{if } z < c \\ a \cdot a_0 \left( \frac{1}{\sqrt{2\pi}s} \right) \exp \left[ -b_r \left( \frac{z-c}{s} \right)^2 \right] + T_{e,plume} - (T_{e,A} - T_{e,plume}) \exp \left[ -b_l \left( \frac{z-c}{s} \right)^2 \right] & \text{if } z > c \end{cases} \quad (30)$$

with  $c = 0.89987$ ,  $s = 0.147529$ ,  $b_l = 1.0238$ ,  $b_r = 0.206867$  and  $a_0 = 0.264274$ . The scaling factor is  $a$ .  $T_{e,A}$  and  $T_{e,plume}$  are, respectively, the electron temperature at the anode and at the near-field plume. Both are chosen parameters. In the simulations presented in this work,  $T_{e,A}$  is set to 4 eV and  $T_{e,plume}$  is set to 3 eV.

## B. Boundary values

In order to solve the algebraic equations and the ODEs found in the model, assumptions on the boundary values of some plasma properties have to be taken.

### 1. Dissociation zone

As far as the dissociation zone is concerned, the following boundary conditions are assumed:

$$n_{I_2,A} = (1 - \xi) \frac{m_{flow}}{m_{I_2} u_{I_2,th} A_{ch}}, \quad (31)$$

$$n_{I,A} = \xi \frac{m_{flow}}{m_I u_{I,th} A_{ch}}, \quad (32)$$

where  $\xi$  accounts for the degree to which part of the iodine

is dissociated by thermalization with the anode walls. It is calculated based on the assumptions of Holbrook et al.<sup>44</sup>. If the simulated HT is xenon-fed, the following neutral density is assumed at the entrance and exit of the dissociation zone:

$$n_{Xe,A} = \frac{m_{flow}}{m_{Xe} u_{Xe,th} A_{ch}}. \quad (33)$$

Neutral velocity is equal at the entrance and exit of the dissociation zone, and is assumed to be a fraction of the thermal velocity:

$$u_{n,th} = 0.4 \sqrt{\frac{8k_B T_n}{\pi m_n}}, \quad (34)$$

with  $n = \{I, I_2\}$  or  $n = \{Xe\}$  and  $T_n$  being set equal to the anode temperature, a set parameter. In the simulations presented in this work,  $T_n$  is set to 750 K. This value is higher than what was estimated from measurements in proximity of the anode. It was however used in light of a potential under-prediction of dissociation, as further detailed in section IV D. It should be mentioned that such a value is inline with what was experimentally found by Mazouffre et al.<sup>45</sup>. Ion density in the dissociation zone is considered constant and equal to that found at the starting boundary of the ionization and acceleration domain. All ions are assumed to exit the dissociation zone with a velocity equal to that of their respective neutral species, thus assuming no electric field is present. Electron temperature in the dissociation zone is assumed constant and is a calibration parameter set to 4 eV.

### 2. Ionization and acceleration zone

As far the ionization and acceleration domain is concerned, the following boundary conditions are assumed:

$$n_{I,in} \text{ and } n_{I_2,in} = \text{calculated in the dissociation zone.} \quad (35)$$

Ion density at the entrance of the domain is considered equal to a fraction of its domain average:

$$n_{ion,in} = \beta_{diss} \bar{n}_{ion}, \quad (36)$$

as mentioned in II. Density of neutrals at the end of the domain is assumed to be a fraction of the domain average:

$$n_{n,out} = 0.001 \bar{n}_n, \quad (37)$$

the ratio based on the results of prior Monte-Carlo simulations<sup>7</sup>. Considering the kinetic energy on an ion accelerated across the domain potential drop:

$$u_{z,\alpha,out} = \sqrt{\frac{2q_e \eta_v \Delta V}{m_\alpha}}, \quad (38)$$

where  $\eta_v$  is the voltage efficiency, and considering the steady-state solution of the conservation of momentum Eq.27, it is possible to assume the density of ions at the end of the domain as:

$$n_{ion,out} = \frac{\bar{n}_{ion}}{2\eta_v}, \quad (39)$$

where the voltage efficiency is a chosen parameter, and has been set to 0.8 in all the simulations presented in this work. Negative ions are assumed to not be present at the boundaries.

Due to the quasi-neutrality assumption, electron density can be derived as:

$$n_{e,in} = \sum_{\alpha} Z_{\alpha} n_{\alpha,in}, \quad (40)$$

$$n_{e,out} = \sum_{\alpha} Z_{\alpha} n_{\alpha,out}. \quad (41)$$

Ion velocity at the end of the domain is derived from the average ion velocity  $\bar{u}_{z,ion}$  and is obtained by using the normalized shape shown in Fig.4.

Neutral velocity at the exit of the acceleration zone is set equal to the sonic velocity:

$$u_{z,n,sonic} = \sqrt{\gamma_n R_n T_n}, \quad (42)$$

where  $\gamma$  is the heat capacity ratio and  $R$  is the specific gas constant.

### C. Calculation of reaction rate

Utilizing the same methodology used to derive 0D equations from a 1D model, one could express the reaction rate term used in continuity and energy equations as:

$$K_{reaction}(\bar{T}_e). \quad (43)$$

This, however, would introduce large inaccuracies, due to the largely non linear nature of reaction rate curves. By using the scalar average electron temperature, reactions with an energy threshold higher than  $\bar{T}_e$  would be largely under-predicted. For these reasons, the normalized electron temperature curve shown in Fig.5 is scaled according the current average electron temperature  $\bar{T}_e$  (which itself is obtained by solving the conservation of electron temperature ODE), the reaction rate is then calculated for each point of the scaled electron temperature curve and then averaged:

$$\bar{K}_{reaction}(T_e(z)), \quad (44)$$

with  $T_e(z)$  being the scaled electron temperature curve. This approximation still provides a global value, but was found to be more accurate at representing the chemistry taking place in the acceleration zone compared to using the spatial average of electron temperature.

## IV. RESULTS

### A. Calculation of performance metrics

The ability of the model to predict global performance of the thruster is evaluated through analysis of expected discharge current and thrust. The former is calculated by sum

of the flux of charged species crossing the boundary at the end of the domain, each weighted by its charge. The sum is then multiplied by channel area. Thrust is calculated as a sum of the momentum flux of each heavy species, multiplied by the channel area  $A_{ch}$  and by a cosine losses factor. Cosine losses account for the effect of beam divergence. They are not predicted by the model and are instead taken as assumption. It has been shown that beam focusing improves with higher anode potential<sup>46</sup>, potentially due to a shift in the position of the acceleration zone<sup>47</sup>. To account for such effect, a simple linear relation is used in calculating the cosine losses factor. In the case of the SPT-100, experimental data are used<sup>46,48</sup>. When the low-power iodine-fed thruster is simulated, a simple linear correlation of divergence with anode potential is also used, with an assumed divergence of 40° at 400 V and of 50° at 200 V, similar to what has been found experimentally for SPT-100. The correlation is kept constant among all the simulated mass flow rates.

### B. Validation against SPT100 data

The model has been initially benchmarked in its xenon version against experimental SPT100 data as extensive information are available regarding this reference thruster<sup>49</sup>. Fig.6 shows discharge current as the anodic mass flow rate is changed, at three different anode potentials. The 0D model systematically over-predicts the experimental results, but successfully captures the trend. The source of the over-prediction may be found in the estimation of the electric field intensity at the end of the domain, described by Eq.12, or in the assumptions regarding anomalous transport. The numerical thrust results are presented in Fig.7 showing quantitative agreement with the experimental data. Fig.8 shows, for an exemplary operating point (anode potential of 300 V and mass flow rate of 4.5 mg s<sup>-1</sup>), how the power injected into the numerical domain is distributed, with a large portion used to accelerate the ions in the beam ( $P_{beam}$ ), a smaller portion delivered to electrons ( $P_E$ ). The latter is then lost to the walls ( $P_{wall}$ ) and used in inelastic collisions ( $P_{coll}$ ). Due to the boundary assump-

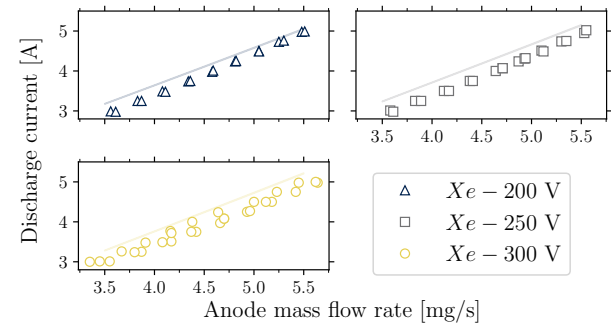


FIG. 6. Experimental (scatter points) and numerical (solid lines) SPT-100 discharge current versus anode mass flow rate at three different anode potentials.

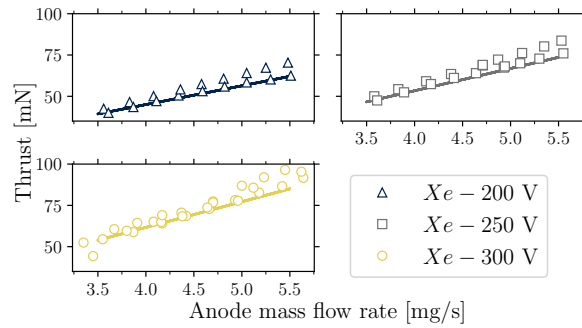


FIG. 7. Experimental and numerical SPT-100 thrust versus anode mass flow rate at three different anode potentials. Scatter points are experimental results, shaded region are numerical results with varying assumed divergences.

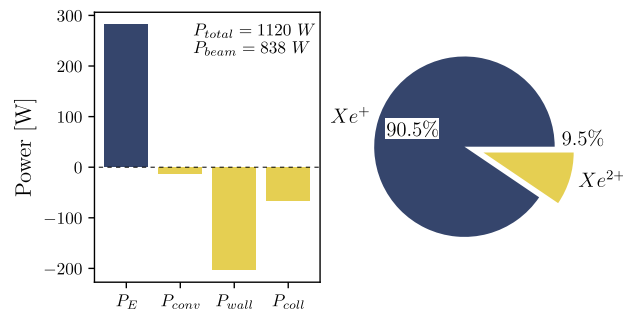


FIG. 8. Power sources and sinks present in the 0D model (left) and predicted beam current composition (right). In this example, the SPT-100 is simulated operating at 300 V with an anodic mass flow of  $4.5 \text{ mg s}^{-1}$ .

tions, a small amount of power ( $P_{conv}$ ) is lost by the stream of electrons leaving the domain, which, even if colder than the electrons entering the domain at the near-field boundary, is much greater in flux. The model finds the total discharge power to be 1272 W, i.e. 10 % above the experimental data. The right side of Fig.8 shows the beam composition, with single charged ions composing the large majority of the beam. This result follows available experimental data, which found single charged ions composed 86% of the beam, followed by doubly charged ions at 13%<sup>50</sup>.

### C. Comparison against iodine-fed HT data

The model has been used to simulate the performance of a low-power iodine-fed HT being developed at ThrustMe, and the numerical results have been compared with experimental data measured at ThrustMe premises. The thruster, named JPT-150, has been designed to function at around 150 W. The thruster was operated at five different anodic mass flow rates, with anode potential sweeping between 200 V and 400 V. During a preliminary performance characterization, filament cathodes have been used as electron source. Facility pressure

was maintained at 1 mPa during operations. Details on the experimental campaign can be found in a separate publication<sup>7</sup>.

Fig.9 shows the discharge current predicted by the 0D model along with the experimental data. Numerical simulations were conducted with varying assumptions on the plasma density in the dissociation zone, by sweeping the  $\beta_{diss}$  parameter between 0.1 (bottom of the shaded areas) and 0.75 (top of the shaded areas). Differently from the xenon-operated SPT-100, higher plasma densities in the dissociation zone have a significant effect on the thrusters performance, causing higher discharge current due to a higher degree of dissociation taking place before the ionization and acceleration zone. As visible in Fig.9, higher dissociation leads to a higher discharge current, due to the larger proportion of individual atoms being ionized. The effect of varying the  $\beta_{diss}$  parameter can also be seen in Fig.10, with the relative proportion of the flux of iodine molecules leaving the domain diminishing as  $\beta_{diss}$  is increased.

When compared to experimental data, it can be noted that the model fails to predict accurately the thruster discharge current, but it grasps the qualitative trend of discharge current, with an error between 5 % and 15 % for all but the smallest mass flow rate, where an error between 30 % and 40 % was found. The source of the error may be attributed to a lack of detailed anomalous transport modeling or to under-prediction of  $I_2$  dissociation leading to a lower estimated discharge current, as indicated by the predicted proportion of the beam composed of ionized molecules being larger than what experimentally measured by Szabo et al.<sup>5</sup>.

The predicted thrust against the anode potential is shown in Fig.11. Due to the nature of the model, assumptions on the divergence half-angle have to be taken, as mentioned in section IV A. The numerical results follow quantitatively the experi-

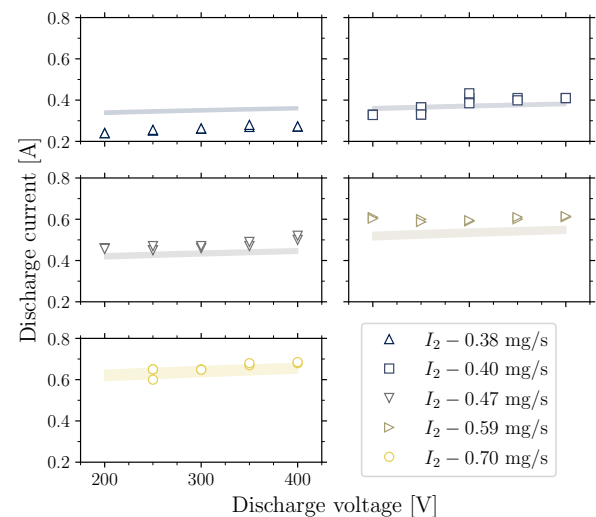


FIG. 9. Discharge current versus discharge potential in JPT-150. Experimental data (scatter points) and numerical data (shaded areas). Numerical results include a sweep of the  $\beta_{diss}$  parameter between 0.1 (bottom shaded area) and 0.75 (top shaded area).

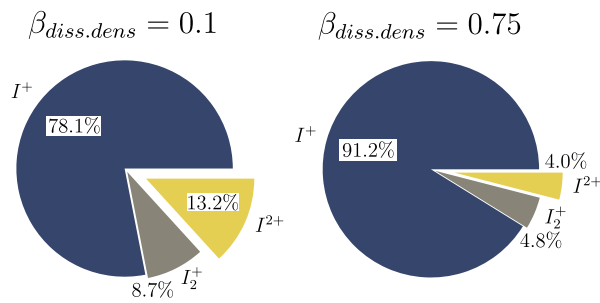


FIG. 10. Predicted beam current composition in JPT-150 operated at 300 V and with anodic mass flow  $0.47 \text{ mg s}^{-1}$ . Plasma density in the dissociation zone is varied through the  $\beta_{diss}$  parameter, set at 0.1 (left) and 0.75 (right).

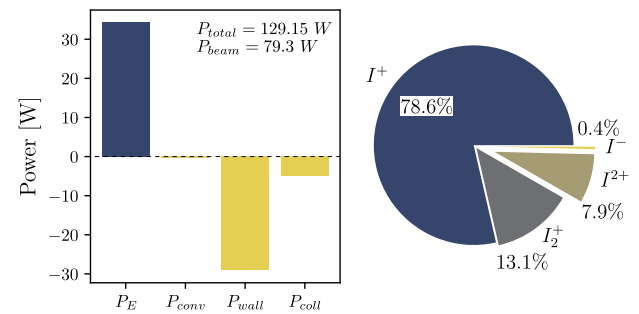


FIG. 12. Power sources and sinks present in the 0D model (left). Predicted bulk plasma densities in the ioniz./accel. zone (right). Case simulated is JPT-150 prototype operating at 300 V with an anodic mass flow rate of  $0.47 \text{ mg s}^{-1}$ .

670 mental results with an average error of 15 %. Fig.12 presents 686  
 672 the distribution of power sources and sinks in the model of the 687  
 673 iodine-fed thruster. A larger fraction of the power is delivered 688  
 674 to the walls via electrons when compared to the results of the 689  
 675 SPT-100 simulation, as expected due to a higher surface-to- 690  
 676 volume ratio as typical of low-power thrusters. Also shown in 691  
 677 Fig.12 is the proportion of bulk plasma densities in the ioniz- 692  
 678 and acceleration zone. It is worth noting the large 693  
 679 proportion of molecular ions, and the presence of negative 694  
 680 ions. More negative ions are expected in the dissociation zone, 695  
 681 where the electron temperature is lower and a larger amount 696  
 682 of iodine molecules are found. The latter is relevant, as disso- 697  
 683 ciative electron attachment is expected to be the main mech- 698  
 684 anism behind the formation of iodine negative ions due to its 699  
 685 large cross section. For the simulation case presented in the

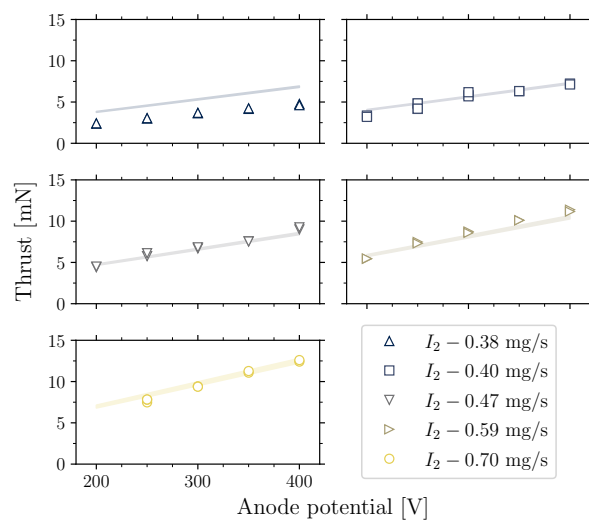


FIG. 11. Thrust versus anode potential in JPT-150. Experimental 717  
 718 data (scatter points) and numerical data (shaded areas). Numerical 719  
 720 results include a sweep of the  $\beta_{diss}$  parameter between 0.1 and 0.75. Divergence is varied linearly with anode potential between half-angle values of  $40^\circ$  and  $50^\circ$ .

figure, the model predicts a bulk density of negative ions of  $6.2 \times 10^{16} \text{ m}^{-3}$  in the dissociation zone and of  $1.5 \times 10^{15} \text{ m}^{-3}$  in the ionization/acceleration zone.

#### D. Presence of negative ions in the dissociation zone

At steady state, the density of negative ions in the dissociation zone is found to approximately be:

$$n_{I^-,diss} \approx \frac{n_{e,diss} \bar{n}_{I_2,diss} K_{DEA}(T_{e,diss})}{n_{e,diss} K_{detach.}(T_{e,diss})}, \quad (45)$$

where  $K_{DEA}$  and  $K_{detach.}$  are the reaction rates for dissociative electron attachment and electron detachment respectively. It can be noted from Eq.45 that the density of negative ions does not depend on electron density directly, and is instead a fraction of the density of iodine molecules present. This fraction depends on the reaction rates involved in the generation and elimination of negative ions and, at  $T_{e,diss} = 4 \text{ eV}$ , is around 0.007. This ratio holds true until a saturation point, where negative ion density approaches plasma density, leading to the formation of an ion-ion plasma. This effect is however unlikely to be physical, given that an ion-ion plasma in proximity of the anode would not be capable of conducting the discharge current, as negative ions lack the mobility to overcome the anode's sheath. Comparing the results with those of other numerical works simulating iodine-fed ICP discharges<sup>9,10</sup>, which do not report this phenomena but make use of similar negative ion collisional sources and sinks, it is believed that the prediction of anomalously high negative ion density is caused by an under-prediction of dissociation and an over-estimation of  $I_2$  density in the dissociation zone. This was accounted for by increasing the ratio between the injected mass flow of iodine atoms and that of iodine molecules artificially by increasing the anode temperature to 750 K, above what was estimated from measurements in proximity of the anode.

Electronegativity in the dissociation zone can be calculated as:

$$\varepsilon = \frac{n_{I^-,diss}}{n_{e,diss}}. \quad (46)$$

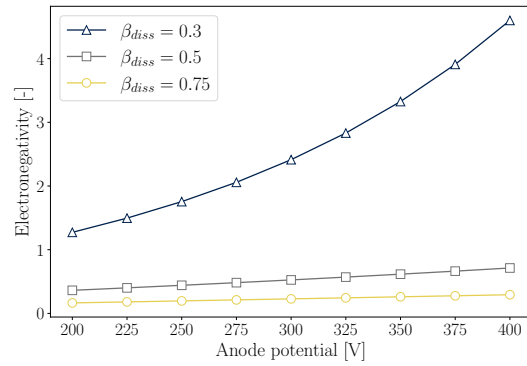


FIG. 13. Electronegativity in the dissociation zone. Case simulated is JPT-150 prototype operating at an anodic mass flow rate of  $0.47 \text{ mg s}^{-1}$ . Electron temperature in dissociation zone is set to  $4 \text{ eV}$ .

Fig.13 shows how higher plasma densities (higher  $\beta_{diss}$ ) lead to a lower electronegativity. Higher plasma densities lead to a larger fraction of  $I_2$  dissociating, and consequently to a reduced amount of negative ions, while at the same time providing a higher amount of electrons. This results in a strong reduction in electronegativity. Anode potential also influences electronegativity in the dissociation zone, with higher anode potentials resulting in lower plasma densities due to higher acceleration of the charged species.

Electron temperature in the dissociation zone was also found to affect electronegativity, especially when set to particularly low values ( $T_{e,diss.} = 2 \text{ eV}$ ), where a large amount of negative ions was predicted. This dependence is due to the previously mentioned ratio of  $K_{DEA}$  and  $K_{detach.}$ . Future work will further analyze this dependence.

The sources to the aforementioned under-estimation of dissociation may be multiple, including further dissociation downstream the injection point caused by collision with the ceramic walls of the channel. Hall thruster with discharge powers similar to those considered in this study have been reported to present wall temperatures between  $570 \text{ K}$  and  $670 \text{ K}$ <sup>51</sup>.

Another potential source of dissociation is photo-dissociation caused by radiation emitted by excited species found in the acceleration zone. The  $I_2$  molecule presents multiple excited states above  $20000 \text{ cm}^{-1}$  that result in dissociation<sup>52,53</sup>. At the same time, neutral atomic iodine  $I$  presents many atomic lines between  $50000 \text{ cm}^{-1}$  and  $70000 \text{ cm}^{-1}$ , indicating that some of the radiation emitted by atoms excited in the hotter ionization and acceleration zones might contribute to the dissociation of molecules deeper in the channel<sup>54</sup>.

## V. CONCLUSION

A global model suitable to analyze iodine-fed Hall thrusters is comprehensively presented. Experimental data from literature has been exploited in order to refine several model as-

sumptions. This approach leads to an innovative Hall thruster global model that differs from other studies previously published enabling relatively accurate prediction capabilities. Iodine chemistry is implemented accounting for  $I_2, I, I^+, I^{2+}, I^-$ . In order to improve the accuracy of molecule dissociation phenomena the domain is divided in two zones, allowing to isolate the low electron temperature environment found in proximity of the anode. The model has been validated against experimental SPT-100 data from the literature. Comparison with experimental data of an iodine-fed Hall thruster prototype developed at ThrustMe is especially addressed and discussed. It was found that thrust generation and discharge current are quantitatively reproduced with an average error of 14 % and 15 %, respectively. With the exception of the lowest mass flow rate case, the thruster discharge current was consistently under-predicted. This inaccuracy is attributed to an under-predicted dissociation of  $I_2$  and to assumptions taken on anomalous transport. Future experimental campaigns will explore the presence of ionized molecules in the thruster plume to further analyze the model capabilities.

## VI. ACKNOWLEDGMENTS

Francesco Mattia Bianchi benefits from a CIFRE PhD (n° 2023/0382) funding grant. The authors want to thank Dmytro Rafalskyi for fruitful discussion during the development of the model and Antoine Poyet for engineering support during the thruster prototype design phase.

## VII. BIBLIOGRAPHY

- M. M. Saravia, L. Bernazzani, A. Ceccarini, A. E. Vinci, and F. Paganucci, "Modeling and Characterization of a Thermally Controlled Iodine Feeding System for Electric Propulsion Applications," *Aerospace* **7**, 10 (2020).
- O. Tverdokhlebov and A. Semenkin, "Iodine propellant for electric propulsion - To be or not to be," in *37th Joint Propulsion Conference and Exhibit* (Salt Lake City, UT, U.S.A., July 2001) AIAA-2001-3350.
- R. Dressler, Y.-H. Chiu, and D. Levandier, "Propellant alternatives for ion and Hall effect thrusters," in *36th AIAA/ASME/SAE/ASEE Aerospace Sciences Meeting and Exhibit* (Huntsville, AL, USA, January 2000) AIAA-2000-0602.
- D. Rafalskyi, J. M. Martínez, L. Habl, E. Zorzoli Rossi, P. Proynov, A. Boré, T. Baret, A. Poyet, T. Lafleur, S. Dudin, and A. Aanesland, "In-orbit demonstration of an iodine electric propulsion system," *Nature* **599**, 411–415 (2021).
- J. Szabo, B. Pote, S. Paintal, M. Robin, A. Hillier, R. D. Branam, and R. E. Huffmann, "Performance Evaluation of an Iodine-Vapor Hall Thruster," *Journal of Propulsion and Power* **28**, 848–857 (2012).
- J. Szabo, M. Robin, S. Paintal, B. Pote, V. Hrubby, and C. Freeman, "Iodine Plasma Propulsion Test Results at 1–10 kW," *IEEE Transactions on Plasma Science* **43**, 141–148 (2015).
- A. E. Vinci, F. M. Bianchi, and D. Rafalski, "Modeling and experimental results of low-power iodine-fed hall thruster propulsion system," in *38th International Electric Propulsion Conference, IEPC 2024-121, Toulouse, France, 23–28 June 2024* (2024).
- P. Grondein, T. Lafleur, P. Chabert, and A. Aanesland, "Global model of an iodine gridded plasma thruster," *Physics of Plasmas* **23**, 033514 (2016).
- B. Esteves, *Investigation of Iodine Plasmas for Space Propulsion Applications*, Ph.D. thesis, Institut Polytechnique de Paris (2023).

This is the author's peer reviewed, accepted manuscript. However, the online version of record will be different from this version once it has been copyedited and typeset. PLEASE CITE THIS ARTICLE AS DOI: 10.1063/5.02444131

- 812 <sup>10</sup>T. Laffleur, L. Habl, E. Z. Rossi, and D. Rafalskyi, "Development and vali-880  
813 dation of an iodine plasma model for gridded ion thrusters," *Plasma Sources*881  
814 *Science and Technology* **31**, 114001 (2022). 882
- 815 <sup>11</sup>T. Laffleur, P. Chabert, and A. Bourdon, "The origin of the breathing mode in883  
816 Hall thrusters and its stabilization," *Journal of Applied Physics* **130**, 053303884  
817 (2021). 885
- 818 <sup>12</sup>L. Leporini, V. Giannetti, S. Camarri, and T. Andreussi, "An unstable886  
819 OD model of ionization oscillations in Hall thruster plasmas," *Frontiers in*887  
820 *Physics*:10.1097813 (2023), 10.3389/fphy.2022.1097813. 888
- 821 <sup>13</sup>E. T. Dale, B. Jorns, and K. Hara, "Numerical investigation of the sta-889  
822 bility criteria for the breathing mode in Hall effect thrusters," in *35th In-*890  
823 *ternational Electric Propulsion Conference, IEPC 2017-265, Atlanta, GA*891  
824 (2017). 892
- 825 <sup>14</sup>K. Hara, M. J. Sekerak, I. D. Boyd, and A. D. Gallimore, en"Perturbation893  
826 analysis of ionization oscillations in Hall effect thrusters," *Physics of Plas-*894  
827 *mas* **21**, 122103 (2014). 895
- 828 <sup>15</sup>M. Nakles, L. Brieda, G. Reed, W. Hargus, and R. Spicer, "Experimental896  
829 and Numerical Examination of the BHT-200 Hall Thruster Plume," in *43rd*897  
830 *AIAA/ASME/SAE/ASEE Joint Propulsion Conference & Exhibit* (American898  
831 Institute of Aeronautics and Astronautics, 2007). 899
- 832 <sup>16</sup>M. M. Saravia, A. Giacobbe, and T. Andreussi, "Bayesian analysis of triple900  
833 Langmuir probe measurements for the characterization of Hall thruster901  
834 plasmas," *Review of Scientific Instruments* **90**, 023502 (2019). 902
- 835 <sup>17</sup>V. Giannetti, M. M. Saravia, L. Leporini, S. Camarri, and T. Andreussi,903  
836 "Numerical and experimental investigation of longitudinal oscillations in904  
837 Hall thrusters," *Aerospace* **8**, 148 (2021). 905
- 838 <sup>18</sup>R. R. Hofer, D. M. Goebel, I. G. Mikellides, and I. Katz, "Magnetic shield-906  
839 ing of a laboratory Hall thruster. II. Experiments," *Journal of Applied*907  
840 *Physics* **115**, 043304 (2014). 908
- 841 <sup>19</sup>J. Szabo and M. Robin, "Plasma Species Measurements in the Plume of an909  
842 Iodine Fueled Hall Thruster," *Journal of Propulsion and Power* **30**, 1357-910  
843 1367 (2014). 911
- 844 <sup>20</sup>J. A. Bittencourt, *Fundamentals of Plasma Physics* (Springer Science &912  
845 Business Media, 2004). 913
- 846 <sup>21</sup>M. K. Scharfe, N. Gascon, M. A. Cappelli, and E. Fernandez, "Comparison914  
847 of hybrid Hall thruster model to experimental measurements," *Physics of*915  
848 *Plasmas* **13**, 083505 (2006). 916
- 849 <sup>22</sup>F. Taccogna and P. Minelli, "Three-dimensional particle-in-cell model of917  
850 Hall thruster: The discharge channel," *Physics of Plasmas* **25**, 061208918  
851 (2018). 919
- 852 <sup>23</sup>E. Ahedo, "Using electron fluid models to analyze plasma thruster dis-920  
853 charges," *Journal of Electric Propulsion* **2**, 2 (2023). 921
- 854 <sup>24</sup>F. Taccogna and L. Garrigues, "Latest progress in Hall thrusters plasma922  
855 modelling," *Reviews of Modern Plasma Physics* **3**, 12 (2019). 923
- 856 <sup>25</sup>R. R. Hofer, *Development and Characterization of High-Efficiency, High-*924  
857 *Specific Impulse Xenon Hall Thrusters*, Ph.D. thesis, University of Michi-925  
858 gan (2004). 926
- 859 <sup>26</sup>V. Kim, "Main Physical Features and Processes Determining the Perfor-927  
860 mance of Stationary Plasma Thrusters," *Journal of Propulsion and Power*928  
861 **14**, 736–743 (1998). 929
- 862 <sup>27</sup>T. R. Hayes, R. C. Wetzel, and R. S. Freund, "Absolute electron-impact-930  
863 ionization cross-section measurements of the halogen atoms," *Physical Re-*931  
864 *view A* **35**, 578–584 (1987). 932
- 865 <sup>28</sup>R. Rejoub, B. G. Lindsay, and R. F. Stebbings, "Determination of the ab-933  
866 solute partial and total cross sections for electron-impact ionization of the934  
867 rare gases," *Physical Review A* **65**, 042713 (2002). 935
- 868 <sup>29</sup>A. Borovik, *Electron-Impact Ionization of Xenon and Tin Ions*, Ph.D. thesis936  
869 University of Giessen (2010). 937
- 870 <sup>30</sup>H. B. Ambalampitiya, K. R. Hamilton, O. Zatsarinny, K. Bartschat, M. A. P.938  
871 Turner, A. Dzarasova, and J. Tennyson, "Electron Scattering Cross-Section939  
872 Calculations for Atomic and Molecular Iodine," *Atoms* **9**, 103 (2021). 940
- 873 <sup>31</sup>H. Yadav, M. Vinodkumar, C. Limbachiya, P. C. Vinodkumar, and N. J. Ma-941  
874 son, "Low energy electron interactions with Iodine molecule (I<sub>2</sub>)," *Journal*942  
875 *of Quantitative Spectroscopy and Radiative Transfer* **250**, 107035 (2020). 943
- 876 <sup>32</sup>"Electron scattering cross section for Xenon atom excitation, Morgan944  
877 database," (2024), www.lxcat.net, Retrieved May 16, 2024. 945
- 878 <sup>33</sup>C. Bélenger, P. Defrance, E. Salzborn, V. Shevelko, H. Tawara, and946  
879 D. Uskov, "Double ionization of neutral atoms, positive and negative ions  
by electron impact," *Journal of Physics B: Atomic, Molecular and Optical*  
*Physics* **30**, 2667 (1999).
- <sup>34</sup>F. Marmuse, *Iodine Plasmas: Experimental and Numerical Studies. Appli-*  
*cation to Electric Propulsion*, Ph.D. thesis, Sorbonne université (2020).
- <sup>35</sup>"Electron scattering cross section for Xenon atom ionization, Hayashi  
database," (2024), www.lxcat.net, Retrieved May 16, 2024.
- <sup>36</sup>M. A. Lieberman and A. J. Lichtenberg, *Principles of Plasma Discharges*  
*and Materials Processing* (John Wiley & Sons, 2005).
- <sup>37</sup>D. M. Goebel and I. Katz, *Fundamentals of Electric Propulsion: Ion and*  
*Hall Thrusters* (John Wiley & Sons, 2008).
- <sup>38</sup>L. Leporini, F. Yaman, T. Andreussi, and V. Giannetti, "Investigation of the  
Effect of Magnetic Field and Propellant on Hall Thruster's Stability via a  
0D Model," *Aerospace* **11**, 227 (2024).
- <sup>39</sup>J. C. Adam, J. P. Boeuf, N. Dubuit, M. Dudeck, L. Garrigues, D. Gresillon,  
A. Heron, G. J. M. Hagelaar, V. Kulaev, N. Lemoine, S. Mazouffre, J. P.  
Luna, V. Pisarev, and S. Tsikata, "Physics, simulation and diagnostics of  
Hall effect thrusters," **50** (2008), 10.1088/0741-3335/50/12/124041.
- <sup>40</sup>S. Mazouffre and G. Bourgeois, "Spatio-temporal characteristics of ion ve-  
locity in a Hall thruster discharge," *Plasma Sources Science and Technology*  
**19**, 065018 (2010).
- <sup>41</sup>S. Mazouffre, D. Pagnon, and J. Bonnet, "Two Ways to Evaluate  
the Xe+ Ion Flow Velocity in a Hall Effect Thruster," in *40th*  
*AIAA/ASME/SAE/ASEE Joint Propulsion Conference and Exhibit* (Ameri-  
can Institute of Aeronautics and Astronautics, Fort Lauderdale, FL, July  
2004) AIAA-2004-3949.
- <sup>42</sup>D. Gawron, S. Mazouffre, N. Sadeghi, and A. Héron, "Influence of mag-  
netic field and discharge voltage on the acceleration layer features in a  
Hall effect thruster," *Plasma Sources Science and Technology* **17**, 025001  
(2008).
- <sup>43</sup>D. Staack, Y. Raitses, and N. J. Fisch, "Temperature gradient in Hall  
thrusters," *Applied Physics Letters* **84**, 3028–3030 (2003).
- <sup>44</sup>R. T. Holbrook and J. A. Kunc, "Impact of dissociation and ionization on  
properties of iodine vapor," *Physics of Plasmas* **1**, 1075–1088 (1994).
- <sup>45</sup>S. Mazouffre, G. Bourgeois, L. Garrigues, and E. Pawelec, "A comprehen-  
sive study on the atom flow in the cross-field discharge of a hall thruster,"  
*Journal of Physics D: Applied Physics* **44**, 105203 (2011).
- <sup>46</sup>M. Nakles, W. Hargus, J. Delgado, and R. Corey, "A Performance and  
Plume Comparison of Xenon and Krypton Propellant on the SPT-100," in  
*48th AIAA/ASME/SAE/ASEE Joint Propulsion Conference* (American Insti-  
tute of Aeronautics and Astronautics, Atlanta, Georgia, July 2012) AIAA-  
2012-4116.
- <sup>47</sup>S. Mazouffre, V. Kulaev, and J. P. Luna, "Ion diagnostics of a discharge  
in crossed electric and magnetic fields for electric propulsion," *Plasma*  
*Sources Science and Technology* **18**, 034022 (2009).
- <sup>48</sup>O. A. Mitrofanova, R. Y. Gnizdor, V. M. Murashko, A. I. Koryakin, and  
A. N. Nesterenko, "New generation of SPT-100," in *32nd International*  
*Electric Propulsion Conference, Wiesbaden, Germany*, Vol. 7 (September  
2011) IEPC-2011-041.
- <sup>49</sup>J. M. Sankovic, J. A. Hamley, and T. W. Haag, "Performance evaluation  
of the Russian SPT-100 thruster at NASA LeRC," in *23rd International*  
*Electric Propulsion Conference* (Seattle, WA, September 1993) IEPC-93-  
094.
- <sup>50</sup>E. E. Barkalov, A. N. Veselovzorov, A. A. Pogorelov, E. B. Svirskii, and  
V. A. Smirnov, "Composition of the beam of an SPT-100 stationary plasma  
thruster," *Instruments and Experimental Techniques* **51**, 263–267 (2008).
- <sup>51</sup>L. Grimaud and S. Mazouffre, "Ion behavior in low-power magnetically  
shielded and unshielded Hall thrusters," *Plasma Sources Science and Tech-*  
*nology* **26**, 055020 (2017).
- <sup>52</sup>R. S. Mulliken, "Iodine Revisited," *The Journal of Chemical Physics* **55**,  
288–309 (2003).
- <sup>53</sup>A. S. Bogomolov, B. Grüner, S. A. Kochubei, M. Mudrich, and A. V. Bak-  
lanov, "Predissociation of high-lying Rydberg states of molecular iodine  
via ion-pair states," *The Journal of Chemical Physics* **140**, 124311 (2014).
- <sup>54</sup>A. Kramida, Yu. Ralchenko, J. Reader, and NIST ASD Team, NIST Atomic Spectra Database (ver. 5.11), [Online]. Available:  
<https://physics.nist.gov/asd> [2024, September 24]. National In-  
stitute of Standards and Technology, Gaithersburg, MD. (2023).